



# GOALS-JWST: Mid-infrared Spectroscopy of the Nucleus of NGC 7469

L. Armus<sup>1</sup>, T. Lai<sup>1</sup>, V. U<sup>2</sup>, K. L. Larson<sup>3</sup>, T. Diaz-Santos<sup>4,5</sup>, A. S. Evans<sup>6,7</sup>, M. A. Malkan<sup>8</sup>, J. Rich<sup>9</sup>, A. M. Medling<sup>10,11</sup>, D. R. Law<sup>12</sup>, H. Inami<sup>13</sup>, F. Muller-Sanchez<sup>14</sup>, V. Charmandaris<sup>4,5,15</sup>, P. van der Werf<sup>16</sup>, S. Stierwalt<sup>17</sup>, S. Linden<sup>18</sup>, G. C. Privon<sup>6,19</sup>, L. Barcos-Muñoz<sup>7</sup>, C. Hayward<sup>20</sup>, Y. Song<sup>6,7</sup>, P. Appleton<sup>1</sup>, S. Aalto<sup>21</sup>, T. Bohn<sup>13</sup>, T. Böker<sup>22</sup>, M. J. I. Brown<sup>23</sup>, L. Finnerty<sup>8</sup>, J. Howell<sup>1</sup>, K. Iwasawa<sup>24,25</sup>, F. Kemper<sup>26,27,28</sup>, J. Marshall<sup>29</sup>, J. M. Mazzarella<sup>1</sup>, J. McKinney<sup>30</sup>, E. J. Murphy<sup>6</sup>, D. Sanders<sup>31</sup>, and J. Surace<sup>1</sup>

<sup>1</sup>IPAC, California Institute of Technology, 1200 East California Boulevard, Pasadena, CA 91125, USA; [lee@ipac.caltech.edu](mailto:lee@ipac.caltech.edu)

<sup>2</sup>Department of Physics and Astronomy, 4129 Frederick Reines Hall, University of California, Irvine, CA 92697, USA

<sup>3</sup>AURA for the European Space Agency (ESA), Space Telescope Science Institute, 3700 San Martin Drive, Baltimore, MD 21218, USA

<sup>4</sup>Institute of Astrophysics, Foundation for Research and Technology-Hellas (FORTH), Heraklion, 70013, Greece

<sup>5</sup>School of Sciences, European University Cyprus, Diogenes Street, Engomi, 1516 Nicosia, Cyprus

<sup>6</sup>National Radio Astronomy Observatory, 520 Edgemont Road, Charlottesville, VA 22903, USA

<sup>7</sup>Department of Astronomy, University of Virginia, 530 McCormick Road, Charlottesville, VA 22903, USA

<sup>8</sup>Department of Physics & Astronomy, 430 Portola Plaza, University of California, Los Angeles, CA 90095, USA

<sup>9</sup>The Observatories of the Carnegie Institution for Science, 813 Santa Barbara Street, Pasadena, CA 91101, USA

<sup>10</sup>Department of Physics & Astronomy and Ritter Astrophysical Research Center, University of Toledo, Toledo, OH 43606, USA

<sup>11</sup>ARC Centre of Excellence for All Sky Astrophysics in 3 Dimensions (ASTRO 3D); Australia

<sup>12</sup>Space Telescope Science Institute, 3700 San Martin Drive, Baltimore, MD 21218, USA

<sup>13</sup>Hiroshima Astrophysical Science Center, Hiroshima University, 1-3-1 Kagamiyama, Higashi-Hiroshima, Hiroshima 739-8526, Japan

<sup>14</sup>Department of Physics and Materials Science, The University of Memphis, 3720 Alumni Avenue, Memphis, TN 38152, USA

<sup>15</sup>Department of Physics, University of Crete, Heraklion, 71003, Greece

<sup>16</sup>Leiden Observatory, Leiden University, PO Box 9513, 2300 RA Leiden, The Netherlands

<sup>17</sup>Physics Department, Occidental College, 1600 Campus Road, Los Angeles, CA 90041, USA

<sup>18</sup>Department of Astronomy, University of Massachusetts at Amherst, Amherst, MA 01003, USA

<sup>19</sup>Department of Astronomy, University of Florida, PO Box 112055, Gainesville, FL 32611, USA

<sup>20</sup>Center for Computational Astrophysics, Flatiron Institute, 162 Fifth Avenue, New York, NY 10010, USA

<sup>21</sup>Department of Space, Earth and Environment, Chalmers University of Technology, SE-412 96 Gothenburg, Sweden

<sup>22</sup>European Space Agency, Space Telescope Science Institute, Baltimore, MD 21218, USA

<sup>23</sup>School of Physics and Astronomy, Monash University, Clayton, VIC 3800, Australia

<sup>24</sup>Institut de Ciències del Cosmos (ICCUB), Universitat de Barcelona (IEEC-UB), Martí i Franquès, 1, E-08028 Barcelona, Spain

<sup>25</sup>ICREA, Pg. Lluís Companys 23, E-08010 Barcelona, Spain

<sup>26</sup>Institut de Ciències de l'Espai (ICE, CSIC), Can Magrans, s/n, E-08193 Bellaterra, Barcelona, Spain

<sup>27</sup>ICREA, Pg. Lluís Companys 23, Barcelona, Spain

<sup>28</sup>Institut d'Estudis Espacials de Catalunya (IEEC), E-08034 Barcelona, Spain

<sup>29</sup>Glendale Community College, 1500 North Verdugo Road, Glendale, CA 91208, USA

<sup>30</sup>Department of Astronomy, University of Massachusetts, Amherst, MA 01003, USA

<sup>31</sup>Institute for Astronomy, University of Hawaii, 2680 Woodlawn Drive, Honolulu, HI 96822, USA

Received 2022 September 26; revised 2022 December 9; accepted 2022 December 12; published 2023 January 13

## Abstract

We present mid-infrared spectroscopic observations of the nucleus of the nearby Seyfert galaxy NGC 7469 taken with the MIRI instrument on the James Webb Space Telescope (JWST) as part of Directors Discretionary Time Early Release Science program 1328. The high-resolution nuclear spectrum contains 19 emission lines covering a wide range of ionization. The high-ionization lines show broad, blueshifted emission reaching velocities up to 1700 km s<sup>-1</sup> and FWHM ranging from ~500 to 1100 km s<sup>-1</sup>. The width of the broad emission and the broad-to-narrow line flux ratios correlate with ionization potential. The results suggest a decelerating, stratified, AGN-driven outflow emerging from the nucleus. The estimated mass outflow rate is 1–2 orders of magnitude larger than the current black hole accretion rate needed to power the AGN. Eight pure rotational H<sub>2</sub> emission lines are detected with intrinsic widths ranging from FWHM ~125 to 330 km s<sup>-1</sup>. We estimate a total mass of warm H<sub>2</sub> gas of ~1.2 × 10<sup>7</sup> M<sub>⊙</sub> in the central 100 pc. The PAH features are extremely weak in the nuclear spectrum, but a 6.2 μm PAH feature with an equivalent width of ~0.07 μm and a flux of 2.7 × 10<sup>-17</sup> W m<sup>-2</sup> is detected. The spectrum is steeply rising in the mid-infrared, with a silicate strength of ~0.02, significantly smaller than seen in most PG QSOs but comparable to other Seyfert 1s. These early MIRI mid-infrared IFU data highlight the power of JWST to probe the multiphase interstellar media surrounding actively accreting supermassive black holes.

*Unified Astronomy Thesaurus concepts:* Active galaxies (17); Starburst galaxies (1570); Infrared galaxies (790)

## 1. Introduction

Luminous infrared galaxies (LIRGs), with thermal IR [8–1000 μm] dust emission in excess of 10<sup>11</sup> L<sub>⊙</sub>, are ideal laboratories for studying star formation and black hole growth in the local universe. The bolometric luminosity of most LIRGs is dominated by massive bursts of star formation but also

shows a wide range of contributions from active galactic nuclei (AGN), which become increasingly important at the highest luminosities (Petric et al. 2011; Stierwalt et al. 2013, 2014). Multiwavelength observations have shown that local LIRGs are a mixture of single disk galaxies, interacting systems, and advanced mergers (Kim et al. 2013; Stierwalt et al. 2013; Larson et al. 2016).

Our understanding of the energetics and evolutionary states of LIRGs at low and high redshifts was greatly expanded through studies with the Infrared Spectrograph (IRS; see Houck et al. 2004) on the Spitzer Space Telescope (see Armus et al. 2020, for a summary). While Spitzer was extremely efficient and capable of deep, as well as large-area, photometric and spectroscopic surveys, it was ultimately limited in sensitivity and spatial resolution by its modest 0.85 m primary mirror. With the successful launch and commissioning of the James Webb Space Telescope (JWST) and its 1–2 orders of magnitude gain in both sensitivity and spatial and spectral resolution over Spitzer, we are now poised to greatly extend our understanding of dusty star-forming regions, nascent AGN, galactic outflows, and all variety of active galaxies over an extremely large stretch of cosmic time. To highlight the power of JWST to explore the inner regions of nearby LIRGs, we have undertaken a Director’s Discretionary Time Early Release Science (ERS) program (1328; PIs: L. Armus, A. S. Evans) to obtain near and mid-infrared images and spectra of four LIRGs drawn from the Great Observatories All-Sky LIRG Survey (GOALS; Armus et al. 2009). GOALS uses multiwavelength observations from the ground and space to understand the physical conditions in over 200 low-redshift ( $z < 0.09$ ) LIRGs selected from the Revised IRAS Bright Galaxy Sample (Sanders et al. 2003). This paper highlights some of the first results from ERS program 1328, “A JWST Study of the Starburst-AGN Connection in Merging Luminous Infrared Galaxies.”

Object NGC 7469 (IRAS 23007+0836; UGC 12332) contains a Seyfert 1.5 nucleus surrounded by a bright, circumnuclear ring of star formation with a radius of  $1''.8$  (580 pc). The total infrared luminosity of NGC 7469 is  $4.5 \times 10^{11} L_{\odot}$ . It is a nearly face-on spiral, about 26 kpc away in projection from an inclined companion galaxy (IC 4283) with a highly disturbed morphology. It has a supermassive black hole (SMBH) mass of  $\sim 10^7 M_{\odot}$ , measured through reverberation mapping (Peterson et al. 2004). The starburst ring is visible at multiple wavelengths, with a large number of star-forming regions having a bimodal age distribution (Díaz-Santos et al. 2007). There is evidence for a highly ionized, outflowing wind on small and large scales (Muller-Sanchez et al. 2011; U et al. 2019; Arav et al. 2020; Robleto-Orus et al. 2021). The mid-infrared Spitzer spectrum of NGC 7469 shows a mix of strong polycyclic aromatic hydrocarbon (PAH) emission features, high-ionization lines, and warm molecular gas indicative of a composite source powered by an active nucleus and a starburst (Inami et al. 2013; Stierwalt et al. 2014). High-resolution observations of CO(1–0), CO(2–1), and [C I] in the inner  $\sim 2$  kpc region with the Atacama Large Millimeter/submillimeter Array (ALMA) show largely rotational kinematics and a large mass of molecular gas (Izumi et al. 2020; Nguyen et al. 2021). With a central AGN, a circumnuclear starburst ring, a high-velocity outflow, and a dusty, gas-rich interstellar medium (ISM), NGC 7469 is an

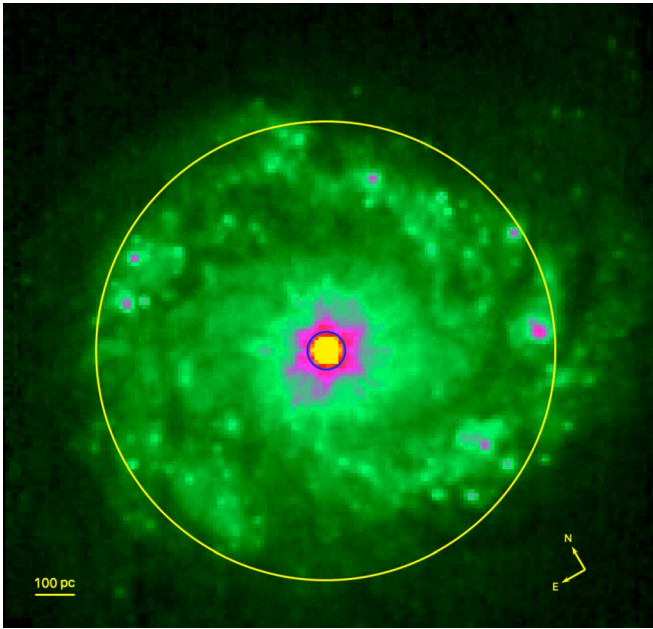
ideal laboratory for studying the coevolution of galaxies and SMBHs at high resolution with JWST.

Here we present JWST integral field spectroscopic observations of the nucleus of NGC 7469 with the Mid-Infrared Instrument (MIRI; Rieke et al. 2015; Labiano et al. 2021). The high spectral–spatial resolution enables us to map the physical properties and kinematics of the atomic and warm molecular gas, as well as the dust on subkiloparsec scales in the mid-infrared for the first time. Specifically, the integral field unit (IFU) data allow us to separately extract and analyze the high signal-to-noise, mid-infrared spectra of the starburst ring, inner ISM, and central AGN. The ring spectra are presented in Lai & Armus (2022). The spectra of the circumnuclear ISM are presented in U et al. (2022). Here we focus on the MIRI spectra of the central active nucleus. Throughout this paper, we adopt  $H_0 = 70 \text{ km s}^{-1} \text{ Mpc}^{-1}$ ,  $\Omega_m = 0.30$ , and  $\Omega_{\text{vac}} = 0.70$ . At the distance of NGC 7469, 70.6 Mpc ( $z = 0.01627$ ),  $1''$  subtends a projected linear scale of 330 pc.

## 2. Observations and Data Reduction

Observations of NGC 7469 were taken with MIRI in Medium Resolution Spectroscopy (MRS) mode on 2022 July 3–4 UT. The observations covered the full 4.9–28.8  $\mu\text{m}$  range using the short (A), medium (B), and long (C) subbands in all four channels. The FASTR1 readout pattern was used to optimize the dynamic range in the observations. The total exposure time per subband was 444 s, using 40 groups per integration and a four-point dither pattern. Because NGC 7469 is extended, dedicated background observations with the same observational parameters in all three grating settings were obtained. MIRI imaging observations were taken using three filters, F560W, F770W, and F1500W, using a cycling three-point dither pattern. Data were collected with both the full imaging field of view ( $74'' \times 113''$ ) and the SUB128 subarray mode ( $14''.1 \times 14''.1$ ) to recover a nonsaturated image of the bright nucleus. The total exposure times are 309, 101, and 101 s and 46, 48, and 48 s for the F560W, F770W, and F1500W filters and full and subarray modes, respectively. The MIRI and NIRCам imaging of the starburst ring in NGC 7469 will be presented in Bohn et al. (2022).

Data for the science and background observations were processed with the JWST Science Calibration Pipeline (Bus-house et al. 2022) version 1.6+ in batch mode. The Detector1 pipeline applies detector-level corrections and ramp fitting to the individual exposures. The output rate images were subsequently processed outside the JWST pipeline to flag newly acquired bad pixels and additional cosmic-ray artifacts and remove the vertical stripes and zero-point residuals remaining after the pipeline dark subtraction. These additional corrections broadly follow the steps taken for JWST Early Release Observation (ERO) observations as described by Pontoppidan et al. (2022). The resulting rate files are then processed with the JWST Spec2 pipeline for distortion and wavelength calibration, flux calibration, and other 2D detector-level steps. Stage 3 processing (Spec3) performs background subtraction before combining data from multiple exposures into the final data cubes. Background light is subtracted from the 2D science images using a master background frame generated from our associated background observations. The master background is a 1D median sigma-clipped spectrum calculated over the field of view of the background observations and projected to the entire 2D detector array. Residual fringe



**Figure 1.** False-color JWST NIRCcam F150W subarray image of the center of NGC 7469. The image, which is  $5''.1$  (1.65 kpc) across, shows the bright, central AGN and the surrounding starburst ring, which is resolved into dozens of star-forming knots, interspersed with regions of diffuse emission and dark dust lanes. In the image, two circles are shown that represent the extraction regions for the MIRI total (large yellow circle;  $3''.6$  diameter) and nuclear (small blue circle;  $0''.3$  diameter) MRS spectra discussed in the text. The total spectrum includes the AGN and starburst ring. The nuclear spectrum is dominated by the AGN and is the focus of this paper. A scale bar depicting 100 pc in projection is shown at the lower left.

corrections using prototype pipeline code have been applied to both the stage 2 products and the 1D spectra resulting from stage 3 processing after spectral extraction (see below).

### 3. Results

We have extracted two spectra from the NGC 7469 MRS data cubes. The first, hereafter the “total” spectrum, is defined as the largest cylindrical aperture that covers the full wavelength extent of MIRI. This aperture has a radius of  $1''.8$  centered on the nucleus. The second extraction, meant to isolate the central AGN, is also centered on the nucleus but with a one FWHM diameter ( $0''.3$  at  $5\ \mu\text{m}$ ) expanding cone. Because this nuclear aperture is fairly small and dominated by the central AGN by design, a wavelength-dependent aperture correction constructed from standard star observations has been applied to the data before measuring emission line fluxes. Both apertures are drawn on the NIRCcam F150W subarray image in Figure 1.

The two NGC 7469 MIRI spectra are shown in Figure 2, along with the low-resolution Spitzer/IRS spectrum from Stierwalt et al. (2013) for comparison. The Spitzer/IRS spectrum is derived from a single pointing on the nucleus with the short-low ( $3''.6$  wide) and long-low ( $10''.5$  wide) slits. As in the Spitzer spectrum, the total NGC 7469 MIRI spectrum is dominated by PAH emission features (complexes) at  $6.2$ ,  $7.7$ ,  $8.6$ ,  $11.3$ , and  $12.6\ \mu\text{m}$ . There are also weaker PAH features seen at  $5.3$ ,  $14.2$ ,  $16.4$ , and  $17.4\ \mu\text{m}$ . Strong, narrow atomic fine-structure emission lines from a variety of species, such as Fe, Ne, Ar, Si, S, O, Mg, and Na, are visible. Emission lines from a number of rotational transitions of warm  $\text{H}_2$  are also seen throughout the spectrum. The brightest of these atomic and molecular gas emission lines were visible in the Spitzer

data, but the MIRI spectra reveal many more lines, and the increased resolving power allows for identification of weak features, clear separation of atomic and molecular gas emission lines from nearby PAH features, and the shapes of the mid-infrared lines and hence the dynamics of the atomic and warm molecular gas to be analyzed in detail for the first time. Some residual fringes and low-level continuum variations are also evident in the total and nuclear spectra near, for example,  $5$ ,  $13$ , and  $25\ \mu\text{m}$  in Figure 2. These may be masking additional faint emission features that will require further analysis with improved versions of the pipeline to confidently measure.

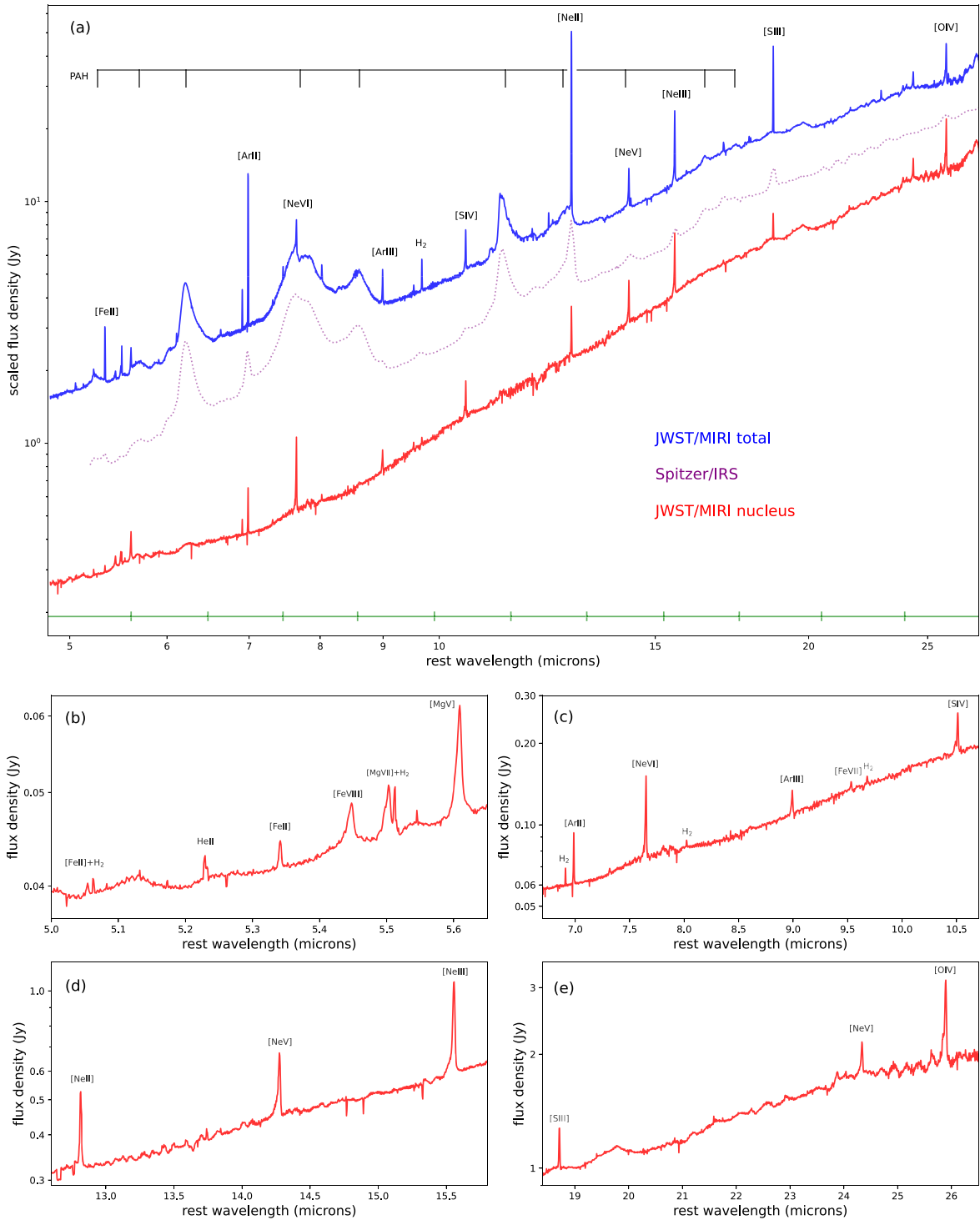
Of particular note is that the NGC 7469 nuclear spectrum shows a striking lack of strong PAH emission and an abundance of high-ionization lines tracing the hard ionizing radiation field emerging from the AGN. The ratios of a number of high- to low-ionization features are clearly enhanced in the nuclear spectrum. There are also eight  $\text{H}_2$  emission lines present in the nuclear spectrum indicative of warm molecular gas. Finally, there is a slight blue upturn in the nuclear spectrum shortward of about  $8\ \mu\text{m}$  that may signal the presence of very warm dust heated by the AGN. The comparison of the two JWST/MIRI spectra demonstrates that in the total spectrum, as in the Spitzer/IRS spectrum, the PAH emission is dominated by the starburst ring, while most of the high-ionization lines (not surprisingly) are coming from the nucleus. The  $\text{H}_2$  emission emerges from the ring and the nucleus. The properties of the outflow and the dust and gas in the starburst ring as traced with MIRI are discussed in U et al. (2022) and Lai & Armus (2022), respectively. Here we concentrate on the properties of the high-resolution nuclear spectrum and what they reveal about the AGN and the wind.

#### 3.1. Ionized Gas

We detect emission lines from the nucleus of NGC 7469 spanning a wide range of ionization states, from  $[\text{Fe II}]$  with  $\text{IP} = 7.9\ \text{eV}$  to  $[\text{Mg VII}]$  with  $\text{IP} = 186.5\ \text{eV}$ , allowing us to explore the properties of the circumnuclear atomic gas as a function of ionization. The coronal lines are very strong in the nucleus of NGC 7469. The  $[\text{Ne V}] 14\ \mu\text{m}/[\text{Ne II}]$  and  $[\text{O IV}]/[\text{Ne II}]$  line flux ratios are 1.5 and 5.0, respectively, comparable to some of the highest values seen in nearby AGN and AGN-dominated LIRGs with ISO and Spitzer (Genzel et al. 1998; Lutz et al. 2000; Sturm et al. 2002; Armus et al. 2007; Tommasin et al. 2010). In some cases, low-ionization emission features are weak or absent from the nuclear spectrum. An example of this is the  $[\text{Fe II}]$  line at  $26\ \mu\text{m}$ . This line is relatively strong in the Spitzer long-high spectrum (Inami et al. 2013), visible but weak in the total MRS spectrum, and not detected in the nuclear MRS spectrum. This likely indicates that most of the flux detected with Spitzer arises on large physical scales, since the projected size of the long-high slit is significantly larger than the extraction region of the total MRS spectrum.

Because of the high spectral resolving power of MIRI, nearly all of the emission lines are resolved in the MRS nuclear spectrum. All lines show a strong narrow component that dominates the emission, while some show a more complex line profile. The narrow line widths, corrected for instrumental broadening, range from  $\sim 100$  to  $400\ \text{km s}^{-1}$ , with a median width of about  $260\ \text{km s}^{-1}$ . While the wavelength calibration is still being refined for MRS and some of the lines have centroids that are clearly offset from their expected positions (e.g., the





**Figure 2.** JWST/MIRI mid-infrared spectra of NGC 7469. The top panel (a) is a comparison of the total MIRI/MRS spectrum (blue solid) and the nuclear extraction (red solid) to the Spitzer/IRS low-resolution spectrum (purple dotted) from Stierwalt et al. (2013). All spectra are arbitrarily scaled and presented in the rest frame. Prominent emission lines and PAH features are labeled at the top. Atomic lines covering a wide range of ionization potentials and a number of  $\text{H}_2$  lines from warm molecular gas are present in the NGC 7469 nuclear spectrum. The PAH features that dominate the total JWST and Spitzer spectra are very weak in the nuclear spectrum, and the high-ionization lines are significantly enhanced relative to the low-ionization lines. The green line at the bottom of the panel indicates the wavelength ranges of individual MIRI/MRS channels. The bottom four panels (b)–(e) highlight four spectral regions of the nuclear spectrum with individual bright emission features labeled. Asymmetric blue wings and broad profiles are evident on many of the high-ionization emission lines, indicative of fast-moving gas associated with a nuclear outflow.

narrow component of the  $[\text{Ne V}]$   $14 \mu\text{m}$  line is blueshifted from its expected position by  $\sim 0.05 \mu\text{m}$ , in many cases (e.g., the narrow component of  $[\text{O IV}]$ ), the centroids of the narrow-line components are consistent with systemic velocity. The

wavelength offsets are channel-dependent, and in the current paper, we refrain from comparing the absolute velocities of lines between channels or to other measurements in the literature.

A large number of the emission line profiles exhibit broad blue wings. This broad emission is prominent in the high-ionization coronal lines (e.g., [Ne V], [Ne VI], and [Mg VII]) but absent from the low-ionization lines (e.g., [Ne II]). The high-velocity emission extends up to  $1700 \text{ km s}^{-1}$  blueward of the narrow component. There is little or no redshifted emission in the high-ionization lines, with the exception of [Mg V]  $5.61 \mu\text{m}$  and [Fe VIII]  $5.447 \mu\text{m}$ , which do show red wings extending out to about  $1000 \text{ km s}^{-1}$ . We have fit all lines that show broad emission with a simple two-component Gaussian model profile to estimate the basic line parameters. In all cases, we have fit a local, linear continuum under each line that extends from about  $\pm 0.1$  to  $0.3 \mu\text{m}$  to mitigate against residual low-level continuum variations. The broad components have FWHMs that range from  $\sim 500$  to  $1000 \text{ km s}^{-1}$ . While we designate these features as broad to facilitate a comparison to the narrow emission, they are far narrower than those from the canonical broad-line region. The FWHM of the  $H\beta$  broad line in NGC 7469 is over  $4300 \text{ km s}^{-1}$  (Peterson et al. 2004). The offsets between the centroids of the narrow and broad components range from  $\sim 100$  to  $600 \text{ km s}^{-1}$ . The fluxes and widths of the narrow and broad components are presented in Table 1, and a subset of the lines are shown scaled and shifted to a common velocity in Figure 3. Because the line is very bright, the broad blueshifted emission in the [O IV] line was also seen in the Spitzer/IRS long-high spectrum of NGC 7469 (Inami et al. 2013), even though the spectral resolving power was only about 550 and the slit was extremely wide (including emission from the disk and starburst ring). The [Ne III] and [Ne V]  $14 \mu\text{m}$  lines were also resolved in the Spitzer spectra, with intrinsic widths of  $\sim 420$  and  $\sim 350 \text{ km s}^{-1}$ , respectively. The centroid of the [Ne V] line was also blueshifted by about  $300 \text{ km s}^{-1}$ . Now that the true line profiles are resolved with JWST, the blueshifts seen in the Spitzer data can be understood as the combined effects of a strong narrow feature near systemic and a broad blue wing.

### 3.2. Warm Molecular Gas

The MIRI MRS spectrum of the nucleus of NGC 7469 reveals the presence of a number of pure rotational emission lines of  $\text{H}_2$  that trace the warm molecular gas in the vicinity of the AGN. Eight transitions are detected in the spectrum, with fluxes ranging from  $\sim 0.5$  to  $5 \times 10^{-18} \text{ W m}^{-2}$ . All of the  $\text{H}_2$  lines are resolved, with intrinsic line widths (FWHM) ranging from  $124$  to  $331 \text{ km s}^{-1}$ —comparable to or less than those of the low-ionization atomic lines. The  $17.05 \mu\text{m}$  S(1) line is the broadest, but its width is highly uncertain. The median line width is  $\sim 210 \text{ km s}^{-1}$  FWHM. None of the  $\text{H}_2$  emission lines show the broad, blueshifted wings seen on the high-ionization atomic emission lines (see Figure 3).

Following Togi & Smith (2016), we have fit the  $\text{H}_2$  line fluxes with a power-law, temperature-dependent excitation function to estimate the characteristic gas temperature and implied mass. The power-law index is 4.55, and there is approximately  $1.3 \times 10^5 M_\odot$  of warm gas at  $T \geq 200 \text{ K}$  and an extrapolated mass (down to  $50 \text{ K}$ ) of  $\sim 1.2 \times 10^7 M_\odot$  in a  $0''.3$  diameter aperture. The latter is approximately 0.4% of the total estimated  $\text{H}_2$  mass within a radius of  $2''.5$  in NGC 7469 (Davies et al. 2004; Izumi et al. 2020) and 18% of the estimated  $\text{H}_2$  mass within a radius of  $0''.2$  (Izumi et al. 2020). The measured S(1)/S(2) line flux ratio is similar to the average value

**Table 1**  
Measured Spectral Features

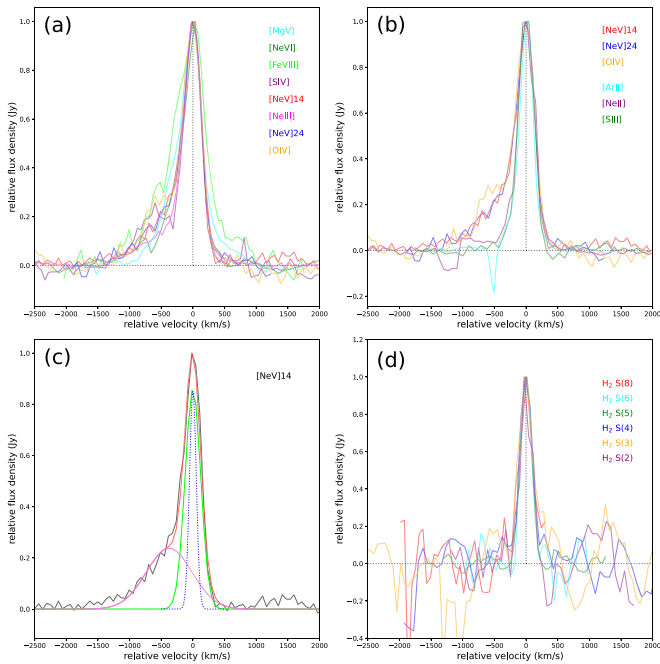
| Feature ID                | $\lambda_{\text{rest}}$<br>( $\mu\text{m}$ ) | IP<br>(eV) | Flux<br>( $10^{-18} \text{ W m}^{-2}$ ) | FWHM<br>( $\text{km s}^{-1}$ ) |
|---------------------------|--|------------|---|--------------------------------|
| 1                         | 2  | 3          | 4                                       | 5                              |
| $\text{H}_2\text{S}(8)$   | 5.053  |            | 0.64 (0.17)                             | 268 (47)                       |
| [Fe II]                   | 5.062  | 7.9        | 0.38 (0.07)                             | <100                           |
| He II                     | 5.228  | 24.6       | 1.29 (0.19)                             | 298 (33)                       |
| [Fe II]                   | 5.340  | 7.9        | 1.31 (0.07)                             | 234 (11)                       |
| [Fe VIII]                 | 5.447  | 124        | 1.98 (0.28)                             | 372 (26)                       |
|                           |  |            | 4.09 (0.36)                             | 1095 (63)                      |
| [Mg VII]                  | 5.503  | 186.5      | 1.03 (0.32)                             | 189 (32)                       |
|                           |  |            | 4.05 (0.42)                             | 621 (36)                       |
| $\text{H}_2 \text{ S}(7)$ | 5.511  |            | 1.45 (0.15)                             | 124 (18)                       |
| [Mg V]                    | 5.610  | 109.2      | 3.51 (0.33)                             | 231 (11)                       |
|                           |  |            | 9.66 (0.41)                             | 726 (22)                       |
| $\text{H}_2\text{S}(6)$   | 6.11   |            | 0.53 (0.05)                             | 175 (12)                       |
| 6.2 PAH                   | 6.22   |            | 27.1 (2.5)                              | ...                            |
| $\text{H}_2\text{S}(5)$   | 6.910  |            | 3.05 (0.11)                             | 188 (5)                        |
| [Ar II]                   | 6.985  | 15.8       | 13.48 (0.61)                            | 261 (10)                       |
| [Na III]                  | 7.318  | 47.3       | 1.76 (0.25)                             | 427 (29)                       |
| [Ne VI]                   | 7.652  | 126.2      | 26.7 (1.99)                             | 309 (13)                       |
|                           |  |            | 18.0 (2.25)                             | 962 (64)                       |
| $\text{H}_2\text{S}(4)$   | 8.025  |            | 1.59 (0.23)                             | 214 (23)                       |
| [Ar III]                  | 8.991  | 27.6       | 7.00 (2.78)                             | 291 (38)                       |
|                           |  |            | 5.31 (1.47)                             | 563 (156)                      |
| [Fe VII]                  | 9.527  | 99.1       | 2.07 (0.69)                             | 237 (34)                       |
|                           |  |            | 2.35 (0.74)                             | 631 (197)                      |
| $\text{H}_2\text{S}(3)$   | 9.665  |            | 2.94 (0.63)                             | 265(43)                        |
| [S IV]                    | 10.511                                       | 34.8       | 22.86 (0.99)                            | 299 (9)                        |
|                           |  |            | 10.9 (1.40)                             | 667 (65)                       |
| $\text{H}_2\text{S}(2)$   | 12.279                                       |            | 2.71 (0.51)                             | 202 (29)                       |
| [Ne II]                   | 12.814                                       | 21.6       | 49.62 (3.62)                            | 313 (14)                       |
| [Ne V]                    | 14.322                                       | 97.1       | 41.77 (3.64)                            | 259 (13)                       |
|                           |  |            | 32.68 (4.51)                            | 814 (62)                       |
| [Ne III]                  | 15.555                                       | 41.0       | 91.61 (4.65)                            | 287 (8)                        |
|                           |  |            | 45.85 (4.79)                            | 920 (38)                       |
| $\text{H}_2\text{S}(1)$   | 17.035                                       |            | 4.16 (1.95)                             | 331 (140)                      |
| [Fe II]                   | 17.936                                       | 7.9        | 2.46 (0.97)                             | 319 (90)                       |
| [S III]                   | 18.713                                       | 23.3       | 46.77 (1.37)                            | 207 (5)                        |
| [Ne V]                    | 24.318                                       | 97.1       | 42.48 (4.07)                            | 224 (12)                       |
|                           |  |            | 34.82 (6.24)                            | 861 (85)                       |
| [O IV]                    | 25.890                                       | 54.9       | 151.73 (26.31)                          | 261 (20)                       |
|                           |  |            | 96.4 (34.61)                            | 706 (165)                      |

**Notes.** Basic properties of the emission lines measured in the JWST/MIRI MRS nuclear spectrum of NGC 7469. Column (1): feature ID; column (2): rest wavelength ( $\mu\text{m}$ ); column (3): line flux ( $10^{-18} \text{ W m}^{-2}$ ); column (4): intrinsic FWHM ( $\text{km s}^{-1}$ ) after subtraction of the instrumental broadening. Lines that have been fit with an additional broad component have a second entry row. The  $1\sigma$  uncertainties in the fitted quantities are given in parentheses. The  $6.2 \mu\text{m}$  emission feature is a series of resolved components, not a single emission line, so it does not have an entry in column (4).

measured by Tommasin et al. (2010) in a sample of Seyfert galaxies with Spitzer.

### 3.3. Dust

The strong PAH features that dominate the total mid-infrared spectrum of NGC 7469 are weak or absent from the nuclear spectrum (see Figure 2). The spectrum does have some residual continuum noise that makes identification of very weak and broad PAH features difficult, but it is clear that the strong PAH emission seen in the total MIRI and Spitzer spectra is not present in the nuclear spectrum. This is consistent with the



**Figure 3.** Atomic and H<sub>2</sub> line profiles in the MIRI/MRS nuclear spectrum of NGC 7469. High-ionization lines are shown in panel (a). A comparison of some of the brighter high- and low-ionization lines is shown in panel (b). All lines are continuum-subtracted and have been normalized and shifted to the centroid of the narrow-line peak. Black dotted lines indicate the base level and zero velocity in each case. The high-ionization lines are all asymmetric, with wings that extend up to 1700 km s<sup>-1</sup> to the blue. The high-velocity blue wings are not present in the low-ionization lines. A simple two-component Gaussian fit to the 14.3 μm [Ne V] line is shown in panel (c). In this panel, the narrow [Ne V] component is in green, the broad blueshifted component is in violet, and the sum is in red. Also shown, with a blue dotted line, is a Gaussian having a width corresponding to an unresolved line at this wavelength. A number of the H<sub>2</sub> emission lines detected in the NGC 7469 nuclear spectrum are shown in panel (d) for comparison. While the H<sub>2</sub> lines are resolved, they are all symmetric and narrow.

results of Lai & Armus (2022) and Honig et al. (2010). We do, however, detect a weak PAH feature at 6.2 μm with a flux of  $\sim 2.7 \pm 0.2 \times 10^{-17}$  W m<sup>-2</sup> and 2.5σ upper limits on the fluxes of the 7.7 and 11.3 μm PAH features of  $\leq 9.2 \times 10^{-17}$  and  $\leq 3.5 \times 10^{-17}$  W m<sup>-2</sup>, respectively. The 6.2 μm nuclear flux is about 0.5% of the PAH emission in the “total” MIRI spectrum. Our 6.2/7.7 PAH flux ratio limit of  $\geq 0.11$  does not allow us to confidently constrain the grain size, but the 6.2 μm PAH equivalent width (EQW) of 0.07 μm is within the range seen for other AGN (e.g., Spoon et al. 2007).

The NGC 7469 nuclear spectrum is steeply rising over much of the MIRI wavelength range with a slight inflection around  $\sim 8$  μm that may signal the presence of warm dust heated by the AGN. The 15-to-5 μm flux density ratio is  $\sim 12.5$ . There is no indication of either strong silicate absorption or emission at 9.7 or 18 μm. The 9.7 μm silicate strength, as defined in Hao et al. (2007), is 0.02. This is smaller than found for many nearby QSOs, where silicate emission is common, and larger than most Seyfert 2s and ULIRGs, where absorption dominates and the silicate strengths are negative but consistent with other Seyfert 1 galaxies observed with Spitzer (Hao et al. 2005, 2007; Schweitzer et al. 2006; Netzer et al. 2007). For comparison, the silicate strength measured in the Spitzer spectrum of NGC 7469 is -0.14, indicative of a small apparent absorption, undoubtedly the result of a significant amount of optically thick dust from the starburst ring within the large Spitzer slit. The silicate

strength, together with the 6.2 μm PAH EQW, places NGC 7469 between class 1A and 1B objects in the diagnostic diagram of Spoon et al. (2007). The low silicate strength, weak PAH EQW, and steep spectral slope may also indicate a contribution from ongoing star formation to the nuclear spectrum (Marshall et al. 2018).

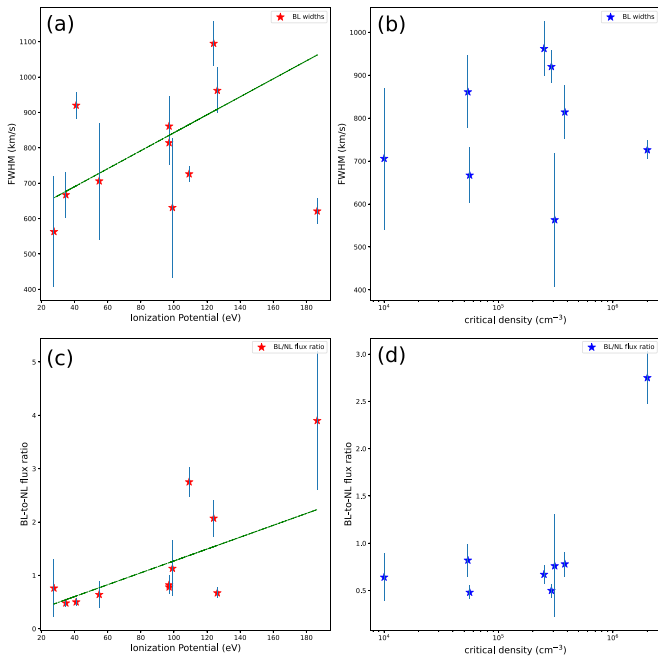
#### 4. Discussion

The high spectral resolution of the MIRI MRS data, together with the range of detected atomic and H<sub>2</sub> lines, allows us to probe the dynamics and ionization structure of the atomic gas and the warm molecular gas in NGC 7469 on scales of  $\sim 100$  pc in the mid-infrared for the first time.

It is known that NGC 7469 has an outflowing, highly ionized nuclear wind seen in the near-infrared [Si VI] coronal line on subarcsecond scales (Muller-Sanchez et al. 2011). The atomic gas measured with MIRI is most likely associated with this outflow. One striking difference, however, is that the MIRI data show gas moving at much higher velocity than mapped in [Si VI], which reaches velocities of  $\pm 120$  km s<sup>-1</sup> at radii of about 0''.2–0''.3. Broad blueshifted emission extending to nearly  $\sim 1000$  km s<sup>-1</sup> is seen in the central spaxel of the Keck/OSIRIS data, but the single Gaussian fits used to construct the outflow model are clearly dominated by slower-moving gas at radii of  $\sim 60$  pc. The high-ionization, high-velocity gas in the JWST MIRI spectrum is also seen as a faint eastern extension in the [Mg V] map produced by U et al. (2022).

The fact that the high-velocity gas is most prominent in the coronal lines is consistent with an ionized, decelerating wind. In this picture, the more highly ionized gas is closer to the AGN and moving at greater speeds. The enhanced blueshifted emission is a result of geometry and possibly extinction, with the receding gas being partially blocked by dust in the inner disk. Despite the high velocities, the bulk of the gas appears to be photoionized, as the [S IV]/[Ne II], the [Ne III]/[Ne II], and the limit on the [Fe II]/[O IV] ratios all imply that shock heating is negligible (Inami et al. 2013). It is likely that the coronal line gas we see in NGC 7469 may also be related to the high-velocity, warm absorber, and emission line gas inferred to exist on much smaller scales (0.1–3 pc) by Grafton-Waters et al. (2020) through modeling of the XMM/RGS spectrum. Blueshifted coronal lines in the mid-infrared have been seen in nearby ULIRGs with powerful outflows (e.g., Spoon & Holt 2009), and it is reminiscent of the kinematic structures seen in some narrow-line Seyfert type 1 galaxies known as “blue outliers” (Komossa et al. 2008), typically identified via asymmetric optical [O III] emission.

To better understand the NGC 7469 outflow probed with MIRI, we plot the broad line widths and broad-to-narrow line flux ratios as a function of ionization potential and critical density in Figure 4. With the exception of the [Mg VII] line at 5.503 μm, which is partially blended with H<sub>2</sub>S(7), the broad line widths show a moderate correlation with ionization potential and the broad-to-narrow line flux ratio (Pearson’s  $r = 0.58$  and 0.57, respectively). There is no correlation with critical density, but this is not surprising, since the ratio of the [Ne V] 14 and 24 μm lines is  $\sim 0.96$  ( $\sim 0.94$  for the broad lines alone), indicating that the coronal line gas is nearly in the low-density limit with  $n_e < 1000$  cm<sup>-3</sup> (see Alexander et al. 1999). The primary correlations of the line widths and relative fluxes are with ionization, similar to what is seen in NGC 1068 (Lutz



**Figure 4.** Emission line properties as a function of ionization and critical density in NGC 7469. The broad line widths and broad-to-narrow component flux ratios are plotted as a function of ionization potential (panels (a) and (c)) and critical density (panels (b) and (d)) for the fine-structure lines in the nuclear spectrum of NGC 7469. The lines show a correlation of broad line width and broad-to-narrow line flux ratio with ionization potential. Linear fits are shown as green dashed lines in panels (a) and (c), excluding the [Mg VII]  $5.5 \mu\text{m}$  line, which is blended with  $\text{H}_2$ .

et al. 2000). The correlations among fit components strengthen the picture of the simple model that is evident from the line profiles alone, namely, that the prominence of the high-velocity, mostly blueshifted gas among the coronal lines seen with MIRI suggests a decelerating, stratified, AGN-driven outflow in NGC 7469.

To estimate the mass outflow rate in the coronal gas, we need to know the gas density, filling factor, maximum velocity, and lateral surface area of the wind. From the [Si VI] emission line map, Muller-Sanchez et al. (2011) estimated a mass outflow rate of  $\sim 4 M_{\odot} \text{yr}^{-1}$ , assuming a density of  $5000 \text{cm}^{-3}$ , filling factor of 0.001, wind lateral surface area of  $11 \times 10^4 \text{pc}^2$ , and maximum velocity of  $130 \text{km s}^{-1}$  (see their Equation 1). If the high-velocity gas we see with JWST emerges in the wind over an area consistent with our aperture and the eastern extension in U et al. (2022), and the gas has a maximum velocity of  $1700 \text{km s}^{-1}$ , density of  $\sim 500 \text{cm}^{-3}$ , and filling factor of 0.001, then we would arrive at a mass outflow rate of  $\sim 0.5\text{--}1 M_{\odot} \text{yr}^{-1}$ . If the gas filling factor is larger, more typical of an AGN narrow-line region (e.g., Storchi-Bergmann et al. 2010), then the outflow rate could be up to  $\sim 5 M_{\odot} \text{yr}^{-1}$ , close to the value estimated by Muller-Sanchez et al. (2011). The mass outflow rate is highly uncertain but still much larger than the gas accretion rate required to power the AGN. Using the scaling between [O IV] and the black hole accretion rate (BHAR) in Stone et al. (2022), we estimate a BHAR of  $\sim 4.1 \times 10^{-2} M_{\odot} \text{yr}^{-1}$ , or roughly 1–2 orders of magnitude less than the mass outflow rate in the ionized wind.

As has been shown by Komossa & Xu (2007), the narrow line widths can be used as a surrogate for the stellar velocity dispersion and therefore used to estimate the black hole mass in Seyfert galaxies, once components associated with any

outflowing gas are removed. While the high-ionization lines show blueshifted emission in the MIRI MRS spectrum of NGC 7469, many of the narrow components have centroids consistent with the systemic velocity. This strong narrow-line component can be used to estimate the mass of the central SMBH, assuming it dominates the dynamical mass in the sampled volume.

Correlations between the widths and luminosities of the mid-infrared [Ne V]  $14.3 \mu\text{m}$  and [O IV]  $25.9 \mu\text{m}$  lines and the mass of the central SMBH were established by Dasyra et al. (2008) using Spitzer/IRS data of a sample nearby Seyfert galaxies, including NGC 7469. Using the width of the narrow component of the [Ne V] and [O IV] lines in the MIRI/MRS nuclear spectrum, we estimate a mass of  $\sim 6 \times 10^6 M_{\odot}$ , about half the value calculated from reverberation line estimates (Peterson et al. 2004) or one-third the value estimated by Nguyen et al. (2021) from fits to the rotating central nuclear disk measured in [C I] and CO with ALMA. We assume here that the shift seen in the [Ne V]  $14.3 \mu\text{m}$  line is due to the wavelength calibration, as described in Section 3.1. Similarly, the luminosities of the narrow lines imply SMBH masses of  $4.4$  and  $4.8 \times 10^7 M_{\odot}$  for [Ne V] and [O IV], respectively, or about a factor of 4–5 larger than the reverberation line estimate. As noted by Dasyra et al. (2008), a large Eddington ratio would lower the SMBH mass predicted from the [O IV] and [Ne V] line luminosities, perhaps bringing them more in line with the reverberation line estimate. By contrast, the widths of the broad components in the MIRI/MRS nuclear spectrum imply SMBH masses that are a factor of 75–80 higher than measured by Peterson et al. (2004). This is consistent with our association of the high-velocity gas with the outflow. Future studies of larger samples of nearby Seyfert galaxies with JWST, where outflowing and infalling gas can be identified and separated with the MIRI and NIRSpect IFUs both spatially and spectrally, could provide a revised calibration of this correlation and a powerful tool to estimate SMBH masses in Seyfert galaxies.

The strong but relatively narrow  $\text{H}_2$  lines in the nuclear spectrum, along with the relatively flat power-law index, suggest that warm molecular gas in the central  $\sim 100 \text{pc}$  is dominated by AGN heating. This is consistent with the relative dip in the line dispersion seen by U et al. (2022) on the nucleus. The fan-shaped structure to the northwest seen as an enhancement in the  $\text{H}_2$  dispersion by U et al. (2022) may reveal a molecular gas shock heated by the wind. The enhanced central [C I] emission has also been suggested as evidence for AGN heating of the circumnuclear gas in an X-ray Dissociation Region (XDR) (Izumi et al. 2020). The near-infrared  $\text{H}_2$  line ratios can be explained by AGN heating or arise in dense gas illuminated by hot stars (Davies et al. 2005). If the  $6.2 \mu\text{m}$  PAH emission seen in the nuclear spectrum is powered by star formation, then the implied star formation rate is  $\sim 0.4 M_{\odot} \text{yr}^{-1}$  (Pope et al. 2008), or less than 1% of the total star formation rate in NGC 7469.

## 5. Summary

We provide an analysis of the high-resolution, mid-infrared spectrum of the nucleus of NGC 7469 taken with the MIRI instrument on board the JWST. The rich set of emission features has provided a detailed picture of the dynamics and physical conditions of the ionized atomic and warm molecular gas and the dust in the inner  $\sim 100 \text{pc}$  of NGC 7469. Our results can be briefly summarized as follows.



1. There are 19 identified emission lines covering a wide range of ionization potential up to 187 eV. The high-ionization lines all show broad, blueshifted emission reaching up to  $-1700 \text{ km s}^{-1}$  with respect to bright, narrow systemic emission. The broad, blueshifted emission is not seen in the low-ionization lines. The width of the broad emission and the broad-to-narrow line flux ratios correlate with ionization potential. We interpret the results as indicative of a decelerating, stratified, AGN-driven outflow emerging from the NGC 7469 nucleus. The estimated mass outflow rate in the wind,  $\sim 1\text{--}5 M_{\odot} \text{ yr}^{-1}$ , is significantly larger than the current black hole accretion rate needed to power the AGN.
2. There are eight pure rotational  $\text{H}_2$  emission lines detected in the nuclear spectrum. The  $\text{H}_2$  lines have a median intrinsic FWHM  $\sim 210 \text{ km s}^{-1}$ , with none showing the broad, blueshifted emission seen in the high-ionization atomic lines. We estimate that there is a total mass of warm gas of  $\sim 1.2 \times 10^7 M_{\odot}$  in the central 100 pc. The high temperature and relatively narrow  $\text{H}_2$  lines in the nuclear spectrum suggest that this warm molecular gas is heated by the AGN.
3. The PAH features that dominate the total mid-infrared spectrum of NGC 7469 are significantly weaker in the nuclear spectrum. We detect a  $6.2 \mu\text{m}$  feature with an EQW  $\sim 0.07 \mu\text{m}$  and a flux of  $2.7 \times 10^{-17} \text{ W m}^{-2}$ . If the PAH emission in the nuclear spectrum is a result of star formation, then the implied star formation rate is  $\sim 0.4 M_{\odot} \text{ yr}^{-1}$ , or less than 1% of the total star formation rate in NGC 7469.
4. The NGC 7469 nuclear spectrum is steeply rising over the MIRI wavelength range. There is no indication of strong silicate absorption or emission at  $9.7 \mu\text{m}$ . The measured silicate strength is 0.02, significantly smaller than found for many nearby QSOs but consistent with other Seyfert 1s.

The mid-infrared nuclear spectrum of NGC 7469 presented here demonstrates the power of MIRI/MRS to disentangle the complex excitation and kinematic properties in the circum-nuclear environments of nearby merging galaxies that are both feeding AGN and rapidly producing stars. These regions are inherently multiphase, and the ability to spatially and spectrally resolve the atomic and molecular gas emission, as well as the dust in these galaxies, is a unique ability made possible with infrared integral field spectrographs on JWST. Planned and future JWST observations of NGC 7469 and other nearby LIRGs and Seyfert galaxies will undoubtedly shed even more light on feeding and feedback at the centers of rapidly evolving galaxies.







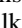





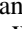
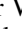
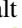




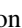




This work is based on observations made with the NASA/ESA/CSA JWST. The research was supported by NASA grant JWST-ERS-01328. The data were obtained from the Mikulski Archive for Space Telescopes at the Space Telescope Science Institute, which is operated by the Association of Universities for Research in Astronomy, Inc., under NASA contract NAS 5-03127 for JWST. The observations can be accessed via <https://doi.org/10.17909/0fe2-cf33>. V.U. acknowledges funding support from NASA Astrophysics Data Analysis Program (ADAP) grant 80NSSC20K0450. The Flatiron Institute is supported by the Simons Foundation. A.M.M. acknowledges support from the National Science Foundation

under grant No. 2009416. A.S.E. and S.L. acknowledge support from NASA grant HST-GO15472. H.I. and T.B. acknowledge support from JSPS KAKENHI grant No. JP21H01129 and the Ito Foundation for Promotion of Science. Y.S. was funded in part by the NSF through the Grote Reber Fellowship Program administered by Associated Universities, Inc./National Radio Astronomy Observatory. F.M.-S. acknowledges support from NASA through ADAP award 80NSSC19K1096. S.A. gratefully acknowledges support from ERC Advanced grant 789410, the Swedish Research Council, and the Knut and Alice Wallenberg (KAW) Foundation. K.I. acknowledges support by the Spanish MCIN under grant PID2019-105510GB-C33/AEI/10.13039/501100011033. This work was also partly supported by the Spanish program Unidad de Excelencia María de Maeztu CEX2020-001058-M, financed by MCIN/AEI/10.13039/501100011033. This research has made use of the NASA/IPAC Extragalactic Database (NED), which is operated by the Jet Propulsion Laboratory, California Institute of Technology, under contract with the National Aeronautics and Space Administration. The National Radio Astronomy Observatory is a facility of the National Science Foundation operated under cooperative agreement by Associated Universities, Inc. The authors would also like to thank an anonymous referee whose comments improved the quality and clarity of this paper.





*Facility:* JWST (NIRCam and MIRI).

*Software:* astropy (Astropy Collaboration et al. 2013, 2018), Cosmology calculator (Wright 2006), JWST Science Calibration Pipeline (Bushouse et al. 2022), CAFE (Marshall et al. 2007, T. Díaz-Santos et al. 2022, in preparation), JDAVis (Lim et al. 2022), lmfit (Newville et al. 2014), Matplotlib (Hunter 2007), Numpy (Van der Walt et al. 2011), QFitsView (Ott 2012), SciPy (Virtanen et al. 2020).

## ORCID iDs

L. Armus  <https://orcid.org/0000-0003-3498-2973>  
T. Lai  <https://orcid.org/0000-0001-8490-6632>  
V. U  <https://orcid.org/0000-0002-1912-0024>  
K. L. Larson  <https://orcid.org/0000-0003-3917-6460>  
T. Díaz-Santos  <https://orcid.org/0000-0003-0699-6083>  
A. S. Evans  <https://orcid.org/0000-0003-2638-1334>  
M. A. Malkan  <https://orcid.org/0000-0001-6919-1237>  
J. Rich  <https://orcid.org/0000-0002-5807-5078>  
A. M. Medling  <https://orcid.org/0000-0001-7421-2944>  
D. R. Law  <https://orcid.org/0000-0002-9402-186X>  
H. Inami  <https://orcid.org/0000-0003-4268-0393>  
F. Muller-Sanchez  <https://orcid.org/0000-0002-2713-0628>  
V. Charmandaris  <https://orcid.org/0000-0002-2688-1956>  
P. van der Werf  <https://orcid.org/0000-0001-5434-5942>  
S. Stierwalt  <https://orcid.org/0000-0002-2596-8531>  
S. Linden  <https://orcid.org/0000-0002-1000-6081>  
G. C. Privon  <https://orcid.org/0000-0003-3474-1125>  
L. Barcos-Muñoz  <https://orcid.org/0000-0003-0057-8892>  
C. Hayward  <https://orcid.org/0000-0003-4073-3236>  
Y. Song  <https://orcid.org/0000-0002-3139-3041>  
P. Appleton  <https://orcid.org/0000-0002-7607-8766>  
S. Aalto  <https://orcid.org/0000-0002-5828-7660>  
T. Bohn  <https://orcid.org/0000-0002-4375-254X>  
T. Böker  <https://orcid.org/0000-0002-5666-7782>  
M. J. I. Brown  <https://orcid.org/0000-0002-1207-9137>  
L. Finnerty  <https://orcid.org/0000-0002-1392-0768>  
J. Howell  <https://orcid.org/0000-0001-6028-8059>



K. Iwasawa  <https://orcid.org/0000-0002-4923-3281>  
 F. Kemper  <https://orcid.org/0000-0003-2743-8240>  
 J. Marshall  <https://orcid.org/0000-0001-7712-8465>  
 J. M. Mazzarella  <https://orcid.org/0000-0002-8204-8619>  
 J. McKinney  <https://orcid.org/0000-0002-6149-8178>  
 E. J. Murphy  <https://orcid.org/0000-0001-7089-7325>  
 D. Sanders  <https://orcid.org/0000-0002-1233-9998>  
 J. Surace  <https://orcid.org/0000-0001-7291-0087>

## References

- Alexander, T., Sturm, E., Lutz, D., et al. 1999, *ApJ*, 512, 204  
 Arav, N., Xu, X., Kriss, G. A., et al. 2020, *A&A*, 633, A61  
 Armus, L., Charmandaris, V., & Soifer, B. T. 2020, *NatAs*, 4, 467  
 Armus, L., Charmandaris, V., Bernard-Salas, J., et al. 2007, *ApJ*, 656, 148  
 Armus, L., Mazzarella, J. M., Evans, A. S., et al. 2009, *PASP*, 121, 559  
 Astropy Collaboration, Robitaille, T. P., Tollerud, E. J., et al. 2013, *A&A*, 558, A33  
 Astropy Collaboration, Price-Whelan, A. M., Sipocz, B. M., et al. 2018, *AJ*, 156, 123  
 Bohn, T., Inami, H., Diaz-Santos, T., et al. 2022, *ApJL*, 941, L36  
 Bushouse, H., Eisenhamer, J., Dencheva, N., et al. 2022, *spacetelescope/jwst: JWST v1.6.2*, Zenodo, doi:10.5281/zenodo.6984366  
 Dasyra, K. M., Ho, L. C., Armus, L., et al. 2008, *ApJL*, 674, L9  
 Davies, R. I., Sternberg, A., Lehnert, M. D., & Tacconi-Garman, L. E. 2005, *ApJ*, 633, 105  
 Davies, R. I., Tacconi, L. J., & Genzel, R. 2004, *ApJ*, 602, 148  
 Díaz-Santos, T., Alonso-Herrero, A., Colina, L., Ryder, S. D., & Knapen, J. H. 2007, *ApJ*, 661, 149  
 Genzel, R., Lutz, D., Sturm, E., et al. 1998, *ApJ*, 498, 579  
 Grafton-Waters, S., Branduardi-Raymont, G., Mehdipour, M., et al. 2020, *A&A*, 633, A62  
 Hao, L., Weedman, D. W., Spoon, H. W. W., et al. 2007, *ApJL*, 655, L77  
 Hao, L., Spoon, H. W. W., Sloan, G. C., et al. 2005, *ApJL*, 625, L75  
 Honig, S. F., Kishimoto, M., Gandhi, P., et al. 2010, *A&A*, 515, A23  
 Houck, J. R., Roellig, T. L., van Cleve, J., et al. 2004, *ApJS*, 154, 18  
 Hunter, J. D. 2007, *CSE*, 9, 90  
 Inami, H., Armus, L., Charmandaris, V., et al. 2013, *ApJ*, 777, 156  
 Izumi, T., Nguyen, D. D., Imanishi, M., et al. 2020, *ApJ*, 898, 75  
 Kim, D. C., Evans, A. S., Vavilkin, T., et al. 2013, *ApJ*, 768, 102  
 Komossa, S., & Xu, D. 2007, *ApJL*, 667, L33  
 Komossa, S., Xu, D., Zhou, H., Storchi-Bergmann, T., & Binette, L. 2008, *ApJ*, 680, 926  
 Labiano, A., Argyriou, I., Álvarez-Márquez, J., et al. 2021, *A&A*, 656, A57  
 Lai, T. S. Y., & Armus, L. 2022, arXiv:2209.06741  
 Larson, K. L., Sanders, D. B., Barnes, J. E., et al. 2016, *ApJ*, 825, 128  
 Lim, P. L., O'Steen, R., Earl, N., et al. 2022, *spacetelescope/jdaviz: v2.8.0*, Zenodo, doi:10.5281/zenodo.6877878  
 Lutz, D., Sturm, E., Genzel, R., et al. 2000, *ApJ*, 536, 697  
 Marshall, J. A., Elitzur, M., Armus, L., Diaz-Santos, T., & Charmandaris, V. 2018, *ApJ*, 858, 59  
 Marshall, J. A., Herter, T. L., Armus, L., et al. 2007, *ApJ*, 670, 129  
 Muller-Sanchez, F., Prieto, M. A., Hicks, E. K. S., et al. 2011, *ApJ*, 739, 69  
 Netzer, H., Lutz, D., Schweitzer, M., et al. 2007, *ApJ*, 666, 806  
 Newville, M., Stensitzki, T., Allen, D. B., & Ingargiola, A. 2014, *LMFIT: Nonlinear Least-Square Minimization and Curve-Fitting for Python v0.8.0*, Zenodo, doi:10.5281/zenodo.11813  
 Nguyen, D. D., Izumi, T., Thater, S., et al. 2021, *MNRAS*, 504, 4123  
 Ott, T. 2012, *QFitsView: FITS file viewer*, Astrophysics Source Code Library ascl:1210.019  
 Peterson, B. M., Ferrarese, L., Gilbert, K. M., et al. 2004, *ApJ*, 613, 682  
 Petric, A. O., Armus, L., Howell, J., et al. 2011, *ApJ*, 730, 28  
 Pontoppidan, K., Blome, C., Braun, H., et al. 2022, *ApJ*, 936, L14  
 Pope, A., Chary, R.-R., Alexander, D. M., et al. 2008, *ApJ*, 675, 1171  
 Rieke, G. H., Wright, G. S., Boker, T., et al. 2015, *PASP*, 127, 584  
 Robbleto-Orus, A. C., Torres-Papaqui, J. P., Longinotti, A. L., et al. 2021, *ApJL*, 906, L6  
 Sanders, D. B., Mazzarella, J. M., Kim, D. C., Surace, J. A., & Soifer, B. T. 2003, *AJ*, 126, 1607  
 Schweitzer, M., Lutz, D., Sturm, E., et al. 2006, *ApJ*, 649, 79  
 Spoon, H. W. W., & Holt, J. 2009, *ApJL*, 702, L42  
 Spoon, H. W. W., Marshall, J. A., Houck, J. R., et al. 2007, *ApJL*, 654, L49  
 Stierwalt, S., Armus, L., Surace, J. A., et al. 2013, *ApJS*, 206, 1  
 Stierwalt, S., Armus, L., Charmandaris, V., et al. 2014, *ApJ*, 790, 124  
 Stone, M., Pope, A., McKinney, J., et al. 2022, *ApJ*, 934, 27  
 Storchi-Bergmann, T., Lopes, R. D. S., McGregor, P. J., et al. 2010, *MNRAS*, 402, 819  
 Sturm, E., Lutz, D., Verma, A., et al. 2002, *A&A*, 393, 821  
 Togi, A., & Smith, J. D. T. 2016, *ApJ*, 830, 18  
 Tommasin, S., Spinoglio, L., Malkan, M. A., & Fazio, G. 2010, *ApJ*, 709, 1257  
 U, V., Medling, A. M., Inami, H., et al. 2019, *ApJ*, 871, 166  
 U, V., Lai, T., Bianchin, M., et al. 2022, *ApJL*, 940, L5  
 Van der Walt, S., Colbert, S. C., & Varoquaux, G. 2011, *CSE*, 13, 22  
 Virtanen, P., Gommers, R., Oliphant, T. E., et al. 2020, *NatMe*, 17, 261  
 Wright, E. L. 2006, *PASP*, 118, 1711